



Article

Enhanced Operational Characteristics Attained by Applying HfO₂ as Passivation in AlGa_N/Ga_N High-Electron-Mobility Transistors: A Simulation Study

Jun-Hyeok Choi¹, Woo-Seok Kang¹, Dohyung Kim¹, Ji-Hun Kim¹, Jun-Ho Lee¹, Kyeong-Yong Kim¹,
Byoung-Gue Min², Dong Min Kang² and Hyun-Seok Kim^{1,*} 

¹ Division of Electronics and Electrical Engineering, Dongguk University-Seoul, Seoul 04620, Republic of Korea; junhyeok6293@dgu.ac.kr (J.-H.C.); kws1117@dongguk.edu (W.-S.K.); ehgudakr@dongguk.edu (D.K.); kjsuk0105@dongguk.edu (J.-H.K.); steve1211@dgu.ac.kr (J.-H.L.); kky0213@dongguk.edu (K.-Y.K.)

² Electronics and Telecommunications Research Institute, Daejeon 34129, Republic of Korea; minbg@etri.re.kr (B.-G.M.); kdm1597@etri.re.kr (D.M.K.)

* Correspondence: hyunseokk@dongguk.edu; Tel.: +82-2-2260-3996

Abstract: This study investigates the operating characteristics of AlGa_N/Ga_N high-electron-mobility transistors (HEMTs) by applying HfO₂ as the passivation layer. Before analyzing HEMTs with various passivation structures, modeling parameters were derived from the measured data of fabricated HEMT with Si₃N₄ passivation to ensure the reliability of the simulation. Subsequently, we proposed new structures by dividing the single Si₃N₄ passivation into a bilayer (first and second) and applying HfO₂ to the bilayer and first passivation layer only. Ultimately, we analyzed and compared the operational characteristics of the HEMTs considering the basic Si₃N₄, only HfO₂, and HfO₂/Si₃N₄ (hybrid) as passivation layers. The breakdown voltage of the AlGa_N/Ga_N HEMT having only HfO₂ passivation was improved by up to 19%, compared to the basic Si₃N₄ passivation structure, but the frequency characteristics deteriorated. In order to compensate for the degraded RF characteristics, we modified the second Si₃N₄ passivation thickness of the hybrid passivation structure from 150 nm to 450 nm. We confirmed that the hybrid passivation structure with 350-nm-thick second Si₃N₄ passivation not only improves the breakdown voltage by 15% but also secures RF performance. Consequently, Johnson's figure-of-merit, which is commonly used to judge RF performance, was improved by up to 5% compared to the basic Si₃N₄ passivation structure.

Keywords: AlGa_N/Ga_N; high-electron-mobility transistor; passivation; HfO₂



Citation: Choi, J.-H.; Kang, W.-S.; Kim, D.; Kim, J.-H.; Lee, J.-H.; Kim, K.-Y.; Min, B.-G.; Kang, D.M.; Kim, H.-S. Enhanced Operational Characteristics Attained by Applying HfO₂ as Passivation in AlGa_N/Ga_N High-Electron-Mobility Transistors: A Simulation Study. *Micromachines* **2023**, *14*, 1101. <https://doi.org/10.3390/mi14061101>

Academic Editors: Zeheng Wang and Jingkai Huang

Received: 27 April 2023

Revised: 22 May 2023

Accepted: 22 May 2023

Published: 23 May 2023



Copyright: © 2023 by the authors. Licensee MDPI, Basel, Switzerland. This article is an open access article distributed under the terms and conditions of the Creative Commons Attribution (CC BY) license (<https://creativecommons.org/licenses/by/4.0/>).

1. Introduction

Generally, AlGa_N/Ga_N high-electron-mobility transistors (HEMTs) are widely adopted in power electronics because of their outstanding electronic and material properties, such as high-critical electric field (~3.3 MV/cm) and wide energy bandgap (3.4 eV). Interestingly, these remarkable characteristics make Ga_N more practicable for high-power and high-frequency applications compared to other materials [1]. Hence, due to these material characteristics, AlGa_N/Ga_N HEMTs exhibit high electron saturation velocity as well as high current density, high thermal reliability, and high breakdown voltage (V_{BD}) [2–4]. In addition, HEMTs based on the AlGa_N/Ga_N heterostructure show admirable performances via a two-dimensional electron gas (2-DEG) in the channel generated by the spontaneous and piezoelectric polarization effects [5,6]. Nevertheless, to sufficiently satisfy the market requirements, Ga_N-based HEMTs require further research for high-voltage and high-frequency applications [7–9]. It has been demonstrated that the field-plate structures in Ga_N-based HEMTs are commonly used to increase the V_{BD}, resulting in operational stability and reliability. However, the frequency characteristics are degraded due to the increase in parasitic capacitances, such as the gate-to-source capacitance (C_{gs}) and gate-to-drain

capacitance (C_{gd}) [10,11]. This clearly shows the advantages and disadvantages of applying field-plates in GaN-based HEMTs due to trade-off between DC and RF characteristics. Additionally, many studies are being conducted to improve the devices' performance [12,13]. As an alternative to HEMTs with field-plate structure, we employed HfO_2 as the passivation to enhance V_{BD} . Interestingly, HfO_2 has a high dielectric constant (~ 25) and large bandgap energy (5.7 eV), both of which may be exploited to improve the devices' performance in comparison with the basic GaN-based HEMTs with Si_3N_4 passivation [14]. Based on these material properties, it is anticipated that the leakage current and V_{BD} characteristics can be improved. However, HfO_2 passivation in HEMTs also produces additional parasitic capacitances, which may degrade their frequency characteristics. Thus, we suggested the additional structures to secure RF performance while applying HfO_2 as a passivation layer.

In this article, we compare and analyze three different passivation structures which use the basic Si_3N_4 , only HfO_2 , and $\text{HfO}_2/\text{Si}_3\text{N}_4$ (hybrid), respectively, as passivation materials. Compared to the basic Si_3N_4 passivation structure, we confirmed that the V_{BD} of the HfO_2 passivation structure improved by approximately 18.8%, but its frequency characteristics were significantly degraded. Meanwhile, the hybrid passivation structure exhibited a slightly reduced V_{BD} , but its frequency characteristics were improved to approximately twice that of the HfO_2 passivation structure. Thus, we optimized the second Si_3N_4 passivation thickness in the hybrid passivation structure to further increase its RF performance. Consequently, the various passivation structures in terms of V_{BD} , on-resistance (R_{on}), and cut-off frequency (f_T) were evaluated using the standard lateral figure-of-merit (LFOM) ($=V_{BD}^2/R_{on}$) and Johnson's figure-of-merit (JFOM) ($=f_T \times V_{BD}$) [15–17].

2. Materials and Methods

To obtain a reasonable simulation criterion, we first analyzed the fabricated HEMT with a 0.15- μm planar-gate structure [18]. The AlGaIn/GaN HEMTs were grown on a 4-inch SiC substrate by using metal-organic chemical vapor deposition. More precisely, the epitaxial layers were composed of a 0.2- μm -thick nucleation layer, a Fe-doped 2- μm -thick GaN buffer layer, and a 25-nm-thick $\text{Al}_{0.25}\text{Ga}_{0.75}\text{N}$ barrier layer. Additionally, the Ohmic metalization of the device was formed by Ti/Al/Ni/Au evaporation followed by rapid thermal annealing at 775 °C for 30 s, and device isolation was achieved by P^+ ion implantation. Next, a 50-nm-thick 1st Si_3N_4 passivation layer was deposited by using plasma-enhanced chemical vapor deposition (PECVD). The first metal interconnections with the Ohmic contacts were formed by the Ti/Au evaporation after etching the 1st Si_3N_4 passivation layer. Further, a planar gate was formed by using single-layer electron beam lithography. More precisely, a gate foot length of 0.15 μm was obtained by electron-beam exposure using poly methyl methacrylate resist, and the 1st Si_3N_4 passivation layer underneath the gate pattern was removed by inductively coupled plasma dry etching. Ni/Au planar-gate metal stack was deposited by electron-beam evaporation and lift-off processes. After this, a 250-nm-thick 2nd Si_3N_4 PECVD film was deposited for device passivation. A source-connected field-plate was formed by using the Ti/Au metal and lift-off process. Finally, the wafer-thinning and backside via-hole process was performed. The scanning electron microscope (SEM) image of the fabricated planar gate AlGaIn/GaN HEMT is shown in Figure 1a.

Figure 1b shows the schematic diagram of the basic Si_3N_4 passivation structure of the HEMT. Based on the fabricated device, we determined the structural and material parameters to be utilized for modeling without any other structural changes, such as changes to the planar-gate electrode structure, and while retaining the same gate foot-length of 0.15 μm , including the epitaxial layer. Table 1 provides the specific geometrical parameter information of the basic Si_3N_4 passivation structure used in the simulation.

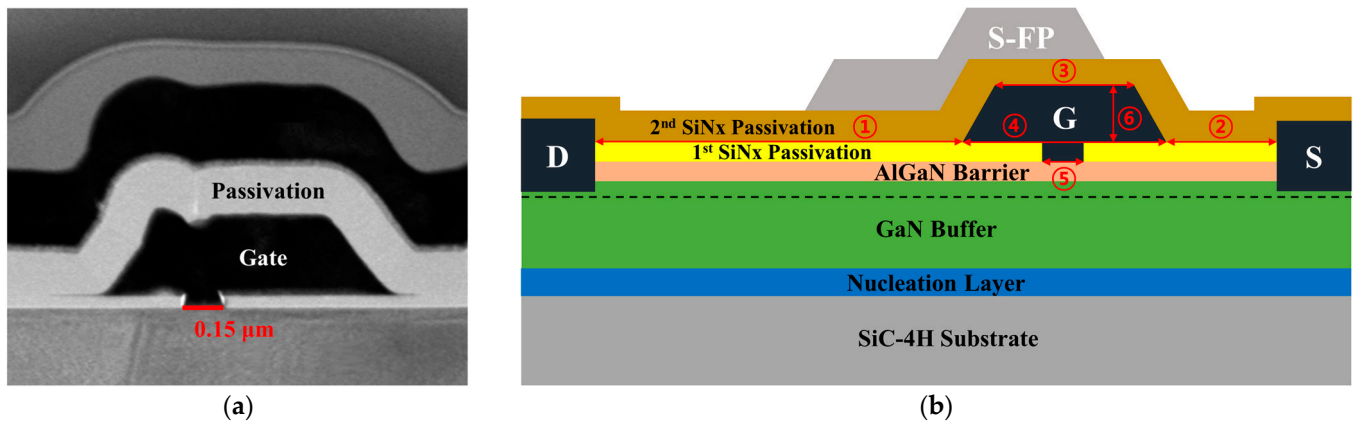


Figure 1. A cross-sectional schematic of the fabricated planar gate AlGaIn/GaN high-electron-mobility transistor (HEMT) structure: (a) scanning electron microscope (SEM) image; and (b) an illustration used in modeling. The S, D, G, and S-FP represent the source, drain, gate, and source-connected field-plate, respectively; each number (1–6) is explained in Table 1.

Table 1. The geometric parameters of the basic Si₃N₄ passivation structure of HEMT.

Parameters	Value (μm)
① L _{Gate–Drain}	1.5
② L _{Gate–Source}	0.5
③ L _{Gate–Head top}	0.8
④ L _{Gate–Head bottom}	1.0
⑤ L _{Gate–Foot}	0.15
⑥ L _{Gate–Height}	0.44
Field-plate thickness	0.44
1st passivation	0.05
2nd passivation	0.25
AlGaIn barrier	0.025
GaN buffer	2
Nucleation layer	0.2

In this simulation study, it is essential to initialize the material and simulation parameters in order to accurately confirm the operating characteristics of the device. The specific material parameters of GaN and AlGaIn used for simulation are summarized in Table 2. As shown in Table 2, we subdivided the FMCT (Farahmand-modified Caughey–Thomas) and GANSAT electron mobility models based on the electric field within the device [19]. Additionally, heat models were applied in the simulation to implement the actual device performance for accurate simulation results. Additionally, acceptor-trap doping in AlGaIn/GaN HEMTs is generally used to improve the V_{BD} by reducing the substrate leakage current [20]. However, current-collapse phenomena such as drain-lag and gate-lag inevitably occur [21]. Therefore, a properly controlled acceptor-trap doping is essential to achieve high-performance HEMTs. The Gaussian acceptor doping profile is applied in the simulation by using Fe (iron). More precisely, the peak acceptor-trap doping concentration is set to $10^{18}/\text{cm}^2$ in the GaN buffer layer and gradually decreases according to the Gaussian distribution, resulting in an acceptor-trap doping concentration below $10^{15}/\text{cm}^2$ at the interface between AlGaIn and GaN.

Table 2. Material parameters used in the simulation at a temperature of 300 K (SRH: Shockley–Read–Hall).

Parameters	Units	GaN	AlGaN
Bandgap energy	eV	3.39	3.88
Electron affinity	eV	4.2	2.3
Relative permittivity	-	9.5	9.38
Low field mobility model	-	FMCT Mobility Model	
High field mobility model	-	GANSAT Mobility Model	
Electron saturation velocity	cm/s	1.9×10^7	1.12×10^7
Hole saturation velocity	cm/s	1.9×10^7	1.00×10^6
Electron SRH lifetime	s	1.0×10^{-8}	1.0×10^{-8}
Hole SRH lifetime	s	1.0×10^{-8}	1.0×10^{-8}

In order to conduct an accurate device simulation by considering the self-heating effect (SHE), we applied physical models to calculate the heat generation within the device [22,23]. First, we used the lattice heat flow equation,

$$C \frac{\partial T_L}{\partial t} = \nabla(\kappa \nabla T_L) + H \quad (1)$$

where C is the heat capacitance per unit volume, κ is the thermal conductivity coefficient, H is the heat generation, and T_L is the local lattice temperature. More precisely, the thermal conductivity, which is important to calculate the SHE in a device simulation, is commonly temperature-dependent. Therefore, we applied the thermal conductivity model,

$$\kappa(T) = (\text{TC.CONST}) / (T_L / 300)^{\text{TC.NPOW}} \quad (2)$$

where TC.CONST is the thermal conductivity constant at 300 K and TC.NPOW is the calibration factor which is an experimental value. The applied TC.CONST and TC.NPOW parameters of GaN, AlGaN, and SiC-4H are summarized in the Table 3 [24].

Table 3. Thermal parameters used for the thermal conductivity model.

Parameters	Units	GaN	AlGaN	SiC-4H
TC.CONST	-	1.3	0.4	3.3
TC.NPOW	-	0.43	0	1.61

We investigated the relationship between parasitic capacitances and frequency characteristics. The capacitance equation can be expressed by:

$$C = \frac{\epsilon_0 \epsilon_r}{d} A \quad (3)$$

where C is the capacitance, ϵ_0 is the permittivity of free space (constant value), ϵ_r is the dielectric constant of the material, A is the area of overlap of the two electrodes, and d is the electrode separation distance. As expressed in Equation (3), ϵ_r and d have a significant influence on the change in capacitance.

Next, f_T and maximum oscillation frequency (f_{\max}) were explained by Equations (4) and (5):

$$f_T = \frac{g_m}{2\pi(C_{gs} + C_{gd})} \approx \frac{g_m}{2\pi C_{gs}} \quad (4)$$

$$f_{\max} = \frac{f_T}{2\sqrt{\pi f_T C_{gd}(R_s + R_g + R_{gs} + 2\pi L_s) + G_{ds}(R_s + R_g + R_{gs} + \pi f_T L_s)}} \approx \sqrt{\frac{f_T}{8\pi R_g C_{gd}}} \quad (5)$$

where g_m , C_{gs} , and C_{gd} represent the transconductance, gate-to-source capacitance, and gate-to-drain capacitance, respectively. As described in Equation (4), decreasing the par-

asitic capacitances, such as C_{gs} and C_{gd} , increases the f_T . The R_s , R_g , R_{gs} , L_s , and G_{ds} are the source resistance, gate resistance, gate-to-source resistance, parasitic source inductance, and output conductance, respectively [25]. Equation (5) shows that R_g and C_{gd} must be reduced to achieve a higher f_{max} . Additionally, as f_T increases, f_{max} also increases, as shown in Equation (5).

3. Results

3.1. Basic Si_3N_4 Passivation Structure of HEMT Modeling Verified by Matching the Simulation's Results with the Measured Data

In this work, we matched the simulated drain current-gate voltage ($I_{DS}-V_{GS}$) transfer and f_T with the measured data of the fabricated basic Si_3N_4 passivation structure of the HEMT to ensure the simulation's reliability. The measured datum of the drain current at a gate voltage of 0 V (I_{dss}) was 898.71 mA/mm, which was similar to the simulated datum of 914.90 mA/mm. Furthermore, the measured maximum transconductance (G_m) was 344.17 mS/mm, which corresponds to the simulated value of 349.60 mS/mm. The above results for maintaining the threshold voltage (V_{th}) at -3.8 V were confirmed. Therefore, by adjusting the simulation's parameters, I_{dss} , G_m , and V_{th} values of the simulation and the corresponding measured results were matched within 1.8% of the maximum error rate, as shown in Figure 2a. A dip of the simulated transconductance around-gate voltage of -2.4 V was found, since two different field-dependent electron mobility models were used, as represented in Table 2. The exact criterion for determining the field within the device as low or high remains unknown, but a slight dip in simulated transconductance can occur at an obscure boundary of these models. The $I_{DS}-V_{GS}$ transfer of the fabricated device was measured by using a Cascade Microtech Summit 12,000 probe station and a HP4142B Modular DC Source/Monitor probe station.

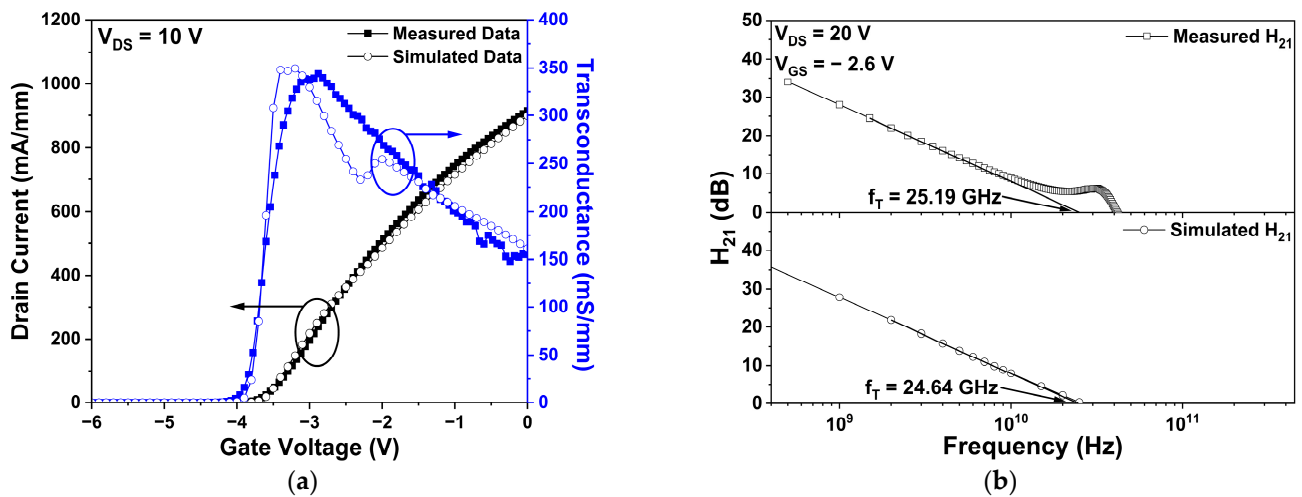


Figure 2. (a) The measured and simulated drain current-gate voltage ($I_{DS}-V_{GS}$) transfer characteristics of a basic Si_3N_4 passivation structure of the HEMT at a drain voltage (V_{DS}) of 10 V. The black and blue arrows represent drain current and transconductance, respectively; and (b) the measured and simulated current gain of a basic Si_3N_4 passivation structure of the HEMT as a function of frequency at $V_{DS} = 20$ V and gate voltage (V_{GS}) = -2.6 V.

The simulated and measured f_T of the basic Si_3N_4 passivation structure of HEMT are shown in Figure 2b. As regards the RF characteristics, the bias points of the simulated results and the measured data were a drain voltage of 20 V and gate voltage of -2.6 V, which were selected since the frequency characteristics were outstanding in comparison to other bias points. More specifically, the f_T was defined as the intersection of the x-axis and the extension line at the point of current gain (H_{21}), with a slope of -20 dB/decade [26]. The measured and simulated values of the f_T were 25.19 GHz and 24.64 GHz, respectively. This

clearly shows that the simulated f_T was accurate enough when compared to the measured values, as the error rate was only 2.2%. PNA-X N5245A network analyzer was used to analyze the f_T of the device within the frequency range from 0.5 to 50 GHz.

3.2. Comparative Analysis between HEMTs with Si_3N_4 , HfO_2 , and Hybrid Passivation Structures

To enhance the operational characteristics, we suggested two structures, as shown in Figure 3. Figure 3a shows the HfO_2 passivation structure of the HEMT. As shown in Figure 3b, the hybrid passivation structure consists of first and second passivation layers, which are composed of HfO_2 and Si_3N_4 , respectively. Specifically, these passivation structures will exhibit enhanced DC characteristics, including the V_{BD} , as compared to the basic Si_3N_4 passivation structure, because of the material properties of HfO_2 . The other structural parameters excluding the passivation material were not changed in the simulation.

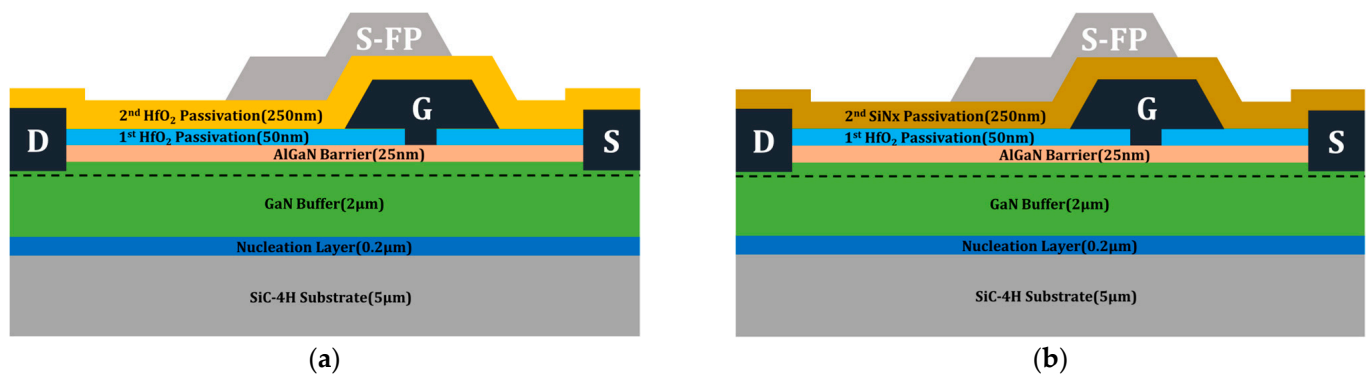


Figure 3. The schematics of various passivation structures for the AlGaN/GaN HEMT: (a) HfO_2 passivation structure; and (b) hybrid passivation structure.

3.2.1. Analysis of DC Characteristics

First, we analyzed the DC characteristics of the HfO_2 and hybrid passivation-structures, and then compared them to the basic Si_3N_4 passivation-structure. Figure 4a shows the $I_{DS}-V_{GS}$ transfer characteristics of all three structures at a drain voltage of 10 V. Among them, the HfO_2 passivation structure slightly improved not only the drain current, but also the transconductance, in comparison with the basic Si_3N_4 passivation structure. Interestingly, these results show that R_{on} decreases as HfO_2 is employed in passivation [27]. The drain current-drain voltage ($I_{DS}-V_{DS}$) characteristics were simulated at the gate voltages of -5 , -4 , -3 , -2 , -1 , and 0 V, respectively, as shown in Figure 4b. As the higher gate voltage was applied, the electron concentration in the channel region increased, resulting in a large drain current. However, a decrease in drain current was observed as the drain voltage increased. These results may be explained by SHE, since applying a higher voltage leads to a higher heat generation, resulting in the degradation of the DC characteristics [28–30]. When the applied drain voltage increased, a strong electric field was generated within the device. Due to the large electric field, phonon scattering was observed to reduce the electron mobility and current density. Although the SHE occurred in all three structures, the HfO_2 passivation and hybrid passivation structures exhibited a higher drain current than did the basic Si_3N_4 passivation structure. In addition, R_{on} was calculated to be 4.02, 3.84, and 3.97 $\Omega\text{-mm}$ for the basic Si_3N_4 , HfO_2 , and hybrid passivation structures, respectively.

Figure 5a shows the electric field distribution in the channel layer under a drain voltage of 200 V. In comparison with the basic Si_3N_4 passivation structure, the HfO_2 and hybrid passivation structures demonstrated that the peak electric field in the channel layer was reduced and dispersed due to the high dielectric constant of HfO_2 . As the peak electric field increased, impact ionization, which causes the generation of electron-hole pairs, became severe. Thus, the redistribution of the electric field effectively improved the V_{BD} . Specifically, the V_{BD} values of the Si_3N_4 , HfO_2 , and hybrid passivation structures were 232.47, 276.27, and 268.41 V, respectively, as shown in Figure 5b. After applying a

voltage of -7 V to the gate to completely turn off the device, the drain voltage when the drain current exceeded 1 mA/mm was defined as the V_{BD} . Figure 5c compares the drain leakage current for the three different passivation structures. Particularly, the structures where HfO_2 is applied to the passivation layer can show that the 2-DEG confinement in the channel region can be improved due to the wide bandgap energy of HfO_2 , reducing the leakage current. Therefore, the HfO_2 passivation structure exhibited the least drain leakage current among the three [31,32].

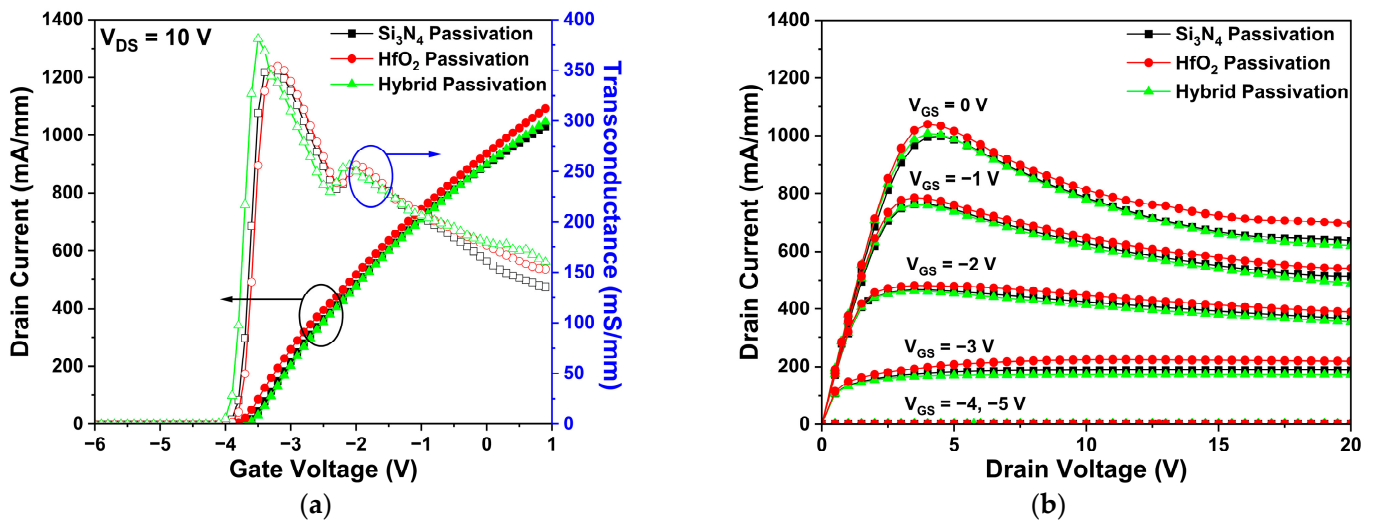


Figure 4. The DC simulation results of Si_3N_4 , HfO_2 , and hybrid passivation structures: (a) I_{DS} - V_{GS} transfer at $V_{DS} = 10\text{ V}$. The black and blue arrows represent drain current and transconductance, respectively; (b) drain current-drain voltage (I_{DS} - V_{DS}) characteristics at $V_{GS} = -5, -4, -3, -2, -1$, and 0 V .

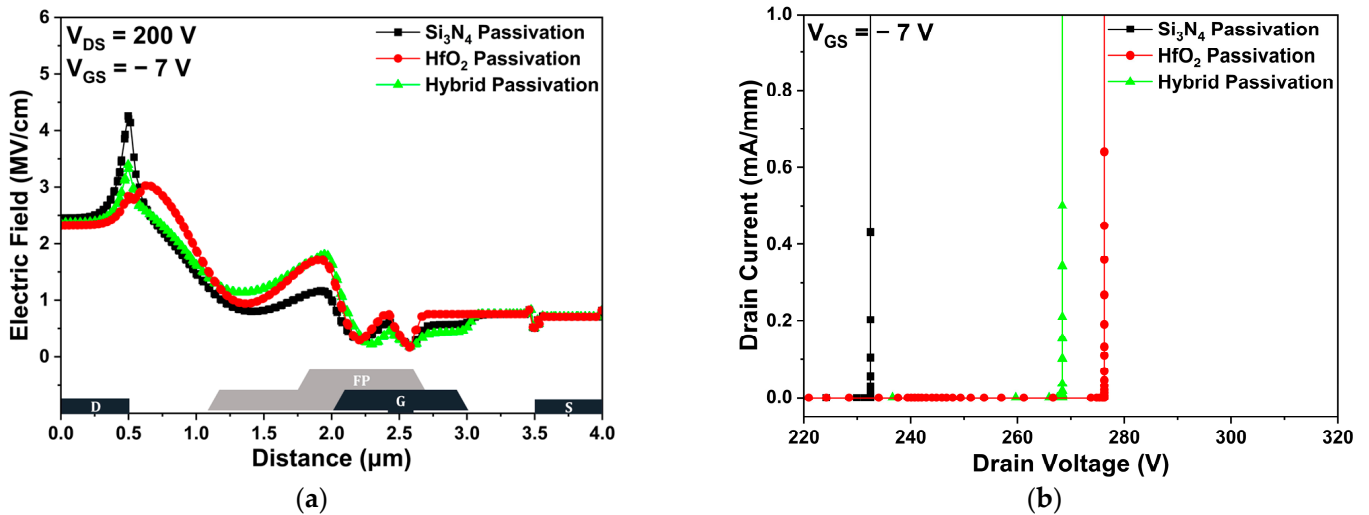


Figure 5. Cont.

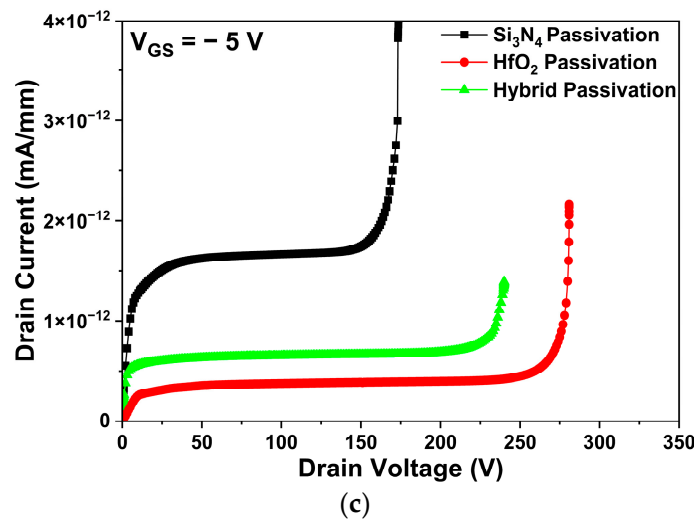


Figure 5. The DC simulation results of Si_3N_4 , HfO_2 , and hybrid passivation structures: (a) electric field distribution in the channel region; (b) off-state breakdown voltage; and (c) off-state drain leakage current.

3.2.2. Analysis of the RF Characteristics

Figure 6 shows the parasitic capacitance characteristics for Si_3N_4 , HfO_2 , and hybrid passivation structures. Specifically, the C_{gs} and C_{gd} were obtained at a drain voltage of 20 V and a gate voltage of -2.6 V. As shown in Figure 6a,b, the HfO_2 passivation structure shows the highest C_{gs} and C_{gd} , since the dielectric constant of HfO_2 is larger than that of Si_3N_4 , which is explained by Equation (3). In addition, the parasitic capacitance values of the hybrid passivation structure were smaller than that of the HfO_2 passivation structure. This is because the HfO_2 passivation thickness was thinner in the hybrid passivation structure compared to the HfO_2 passivation structure. Therefore, the parasitic capacitances tended to increase as more HfO_2 was used in the passivation layer.

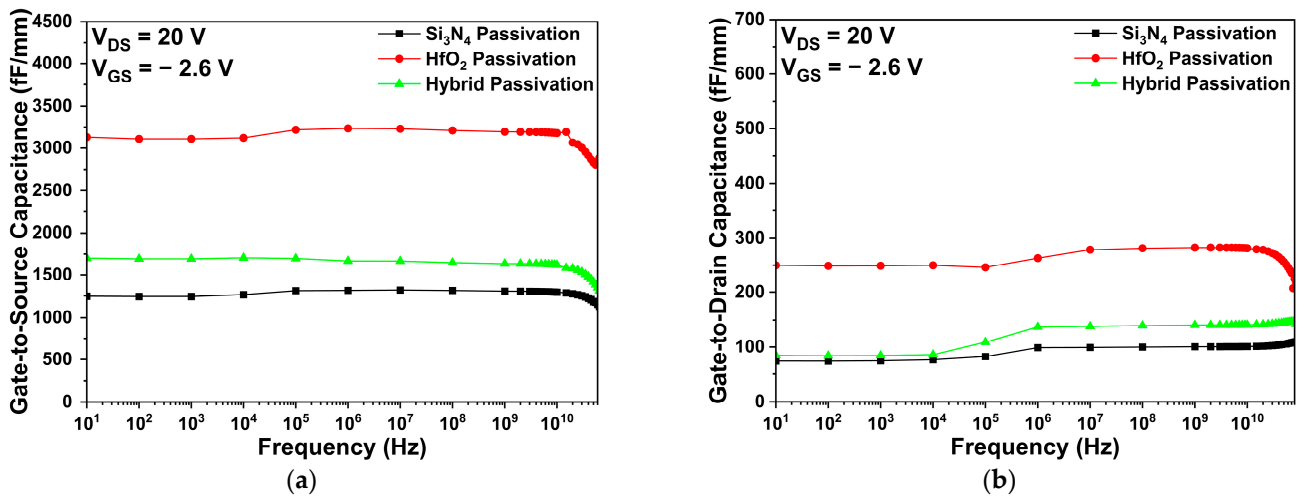


Figure 6. The parasitic capacitance characteristics of Si_3N_4 , HfO_2 , and hybrid passivation structures: (a) gate-to-source capacitance; and (b) gate-to-drain capacitance.

Figure 7 represents the simulated f_T and f_{max} of the three different passivation structures. Similarly, as the capacitance simulations, f_T and f_{max} , were obtained at a drain voltage of 20 V and a gate voltage of -2.6 V. More precisely, the f_T values are 24.64, 10.17, and 20.50 GHz for the basic Si_3N_4 passivation, HfO_2 passivation, and hybrid passivation structures, respectively. The f_T values of the HfO_2 and hybrid passivation structures

were decreased by 58.7% and 16.8% compared to the basic Si_3N_4 passivation structure, respectively. According to Equation (4), the f_T values of the three passivation structures may have been influenced by the g_m and C_{gs} . In addition, the f_{max} values of the basic Si_3N_4 passivation, HfO_2 passivation, and hybrid passivation structures are 110.28, 48.72, and 88.53 GHz, respectively. It can be seen that f_{max} value of HfO_2 passivation structure significantly decreased as f_T decreased according to Equation (5). Particularly, the f_{max} , which is obtained from the extension line with a slope of -20 dB/decade at the intersection of the maximum stable/available gain (MSG/MAG), becomes 0 dB [33,34].

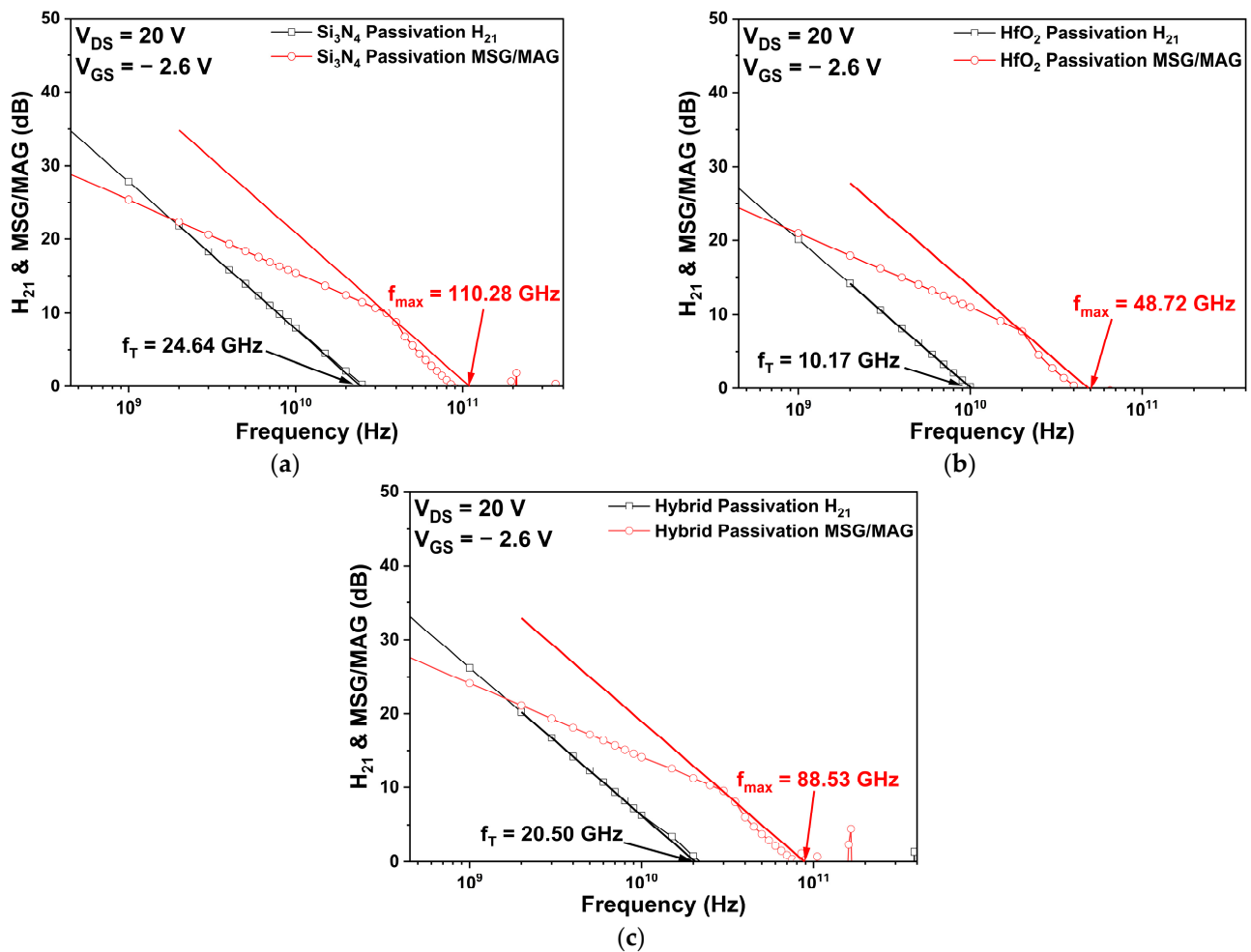


Figure 7. The cut-off frequency (f_T) and maximum oscillation frequency (f_{max}) for different passivation structures: (a) Si_3N_4 passivation structure; (b) HfO_2 passivation structure; and (c) hybrid passivation structure.

Interestingly, these results clearly show that the ratio of HfO_2 in passivation is important for DC and RF performances. As the ratio of HfO_2 increases, the DC characteristics are improved, but the RF characteristics, such as parasitic capacitances and frequency characteristics, are degraded due to the material properties of HfO_2 . To improve both DC and RF characteristics, we selected the hybrid passivation structure and then simulated four different 2nd Si_3N_4 passivation thicknesses, i.e., 150, 250, 350, and 450 nm, which will be discussed in Section 3.3. More precisely, to optimize the second Si_3N_4 passivation thickness and calculate the figure-of-merit, we analyzed the operational characteristics including V_{BD} , parasitic capacitances, and frequency characteristics.

3.3. Determination of the Optimum Second Passivation Thickness for Hybrid Structure

3.3.1. Analysis of the DC Characteristics

Figure 8a shows the electric field distribution in the channel region at a drain voltage of 200 V and a gate voltage of -7 V. The peak electric field was not significantly affected by the second passivation thickness. Additionally, the overall electric field distribution also showed no significant difference. Therefore, the V_{BD} values of the various second passivation thickness structures were not changed significantly. As shown in Figure 8b, the V_{BD} was simulated to be 262.00, 268.41, 267.57, and 262.30 V for the hybrid passivation structure with second passivation thicknesses of 150, 250, 350, and 450 nm, respectively. As the field-plate gradually deviates from the channel region, the electric field in the channel cannot be dispersed, resulting in the decrease of V_{BD} . Meanwhile, as the passivation thickness increases, it is expected that V_{BD} would increase, because the passivation can prevent the electric field in the channel region spread by the high electric field adjacent to the gate electrode. For these two reasons, the V_{BD} were slightly enhanced in the second passivation thicknesses of 250 and 350 nm, compared with other structures.

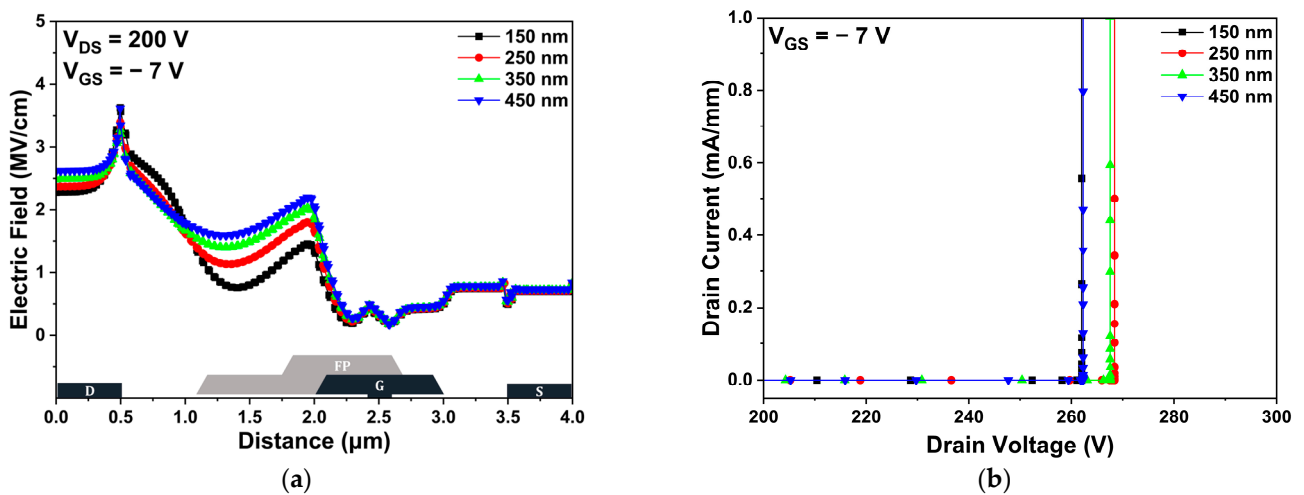


Figure 8. The DC simulation results of hybrid passivation structure with various second passivation thicknesses: (a) electric field distribution in the channel region; and (b) off-state breakdown voltage.

3.3.2. Analysis of the RF Characteristics

Figure 9 shows the C_{gs} and C_{gd} of the hybrid passivation structure with various second passivation thicknesses, at a drain voltage of 20 V and a gate voltage of -2.6 V. The second passivation thickness affected the parasitic capacitance values. Specifically, the 150-nm-thick second passivation structure showed the largest C_{gs} , due to the decrease in distance between the gate and source, as shown in Figure 9a. According to Equation (3), as the distance among the electrodes increased, the parasitic capacitances decreased. Therefore, compared to C_{gs} , there is no significant change in C_{gd} , because the gate-to-source distance is much shorter than the gate-to-drain distance. In addition, the 450-nm-thick second passivation structure exhibited a slightly larger C_{gd} than did the other structures, as shown in Figure 9b. The change in materials from air to Si_3N_4 led to an increase in C_{gd} due to dielectric constant of the materials, which is explained by Equation (3).

Figure 10 shows the simulated f_T and f_{max} values for the different second passivation thicknesses at a drain voltage of 20 V and a gate voltage of -2.6 V. When the second passivation thicknesses were 150, 250, 350, and 450 nm, the f_T values in the simulations were 17.92, 20.50, 22.64, and 24.97 GHz, respectively. A decrease in the C_{gs} due to a change in the second passivation thickness led to an increase in f_T , according to Equation (4). Therefore, f_T tended to increase by about 14.4~39.3% as the second passivation thickness was extended by each 100-nm-step. The f_{max} values were simulated to be 78.50, 88.53, 91.47, and 106.39 GHz for the hybrid passivation structure with the second passivation

thicknesses of 150, 250, 350, and 450 nm, respectively. Comparing the f_{max} values of the hybrid passivation structures based on the different second passivation thicknesses, it can be demonstrated that the f_{max} values increased by 12.8~35.5% with each 100-nm-step increase in the second passivation thickness. According to Equation (5), the f_{max} values were mainly influenced by the increase in f_T because there was no significant change in C_{gd} . Throughout these results, we confirmed the dependence of frequency characteristics in relation to the second passivation thickness.

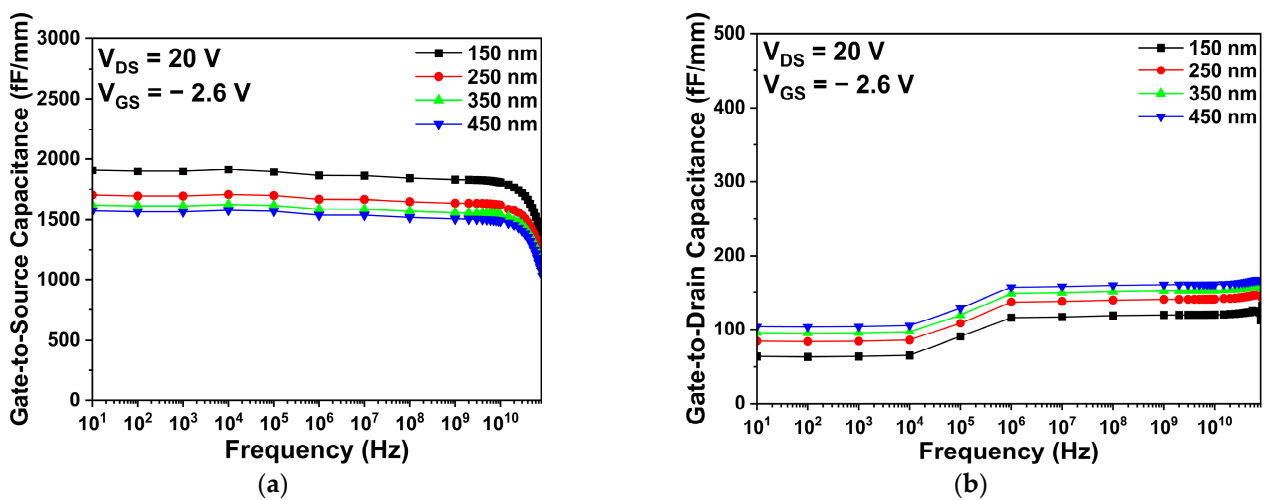


Figure 9. The parasitic capacitance characteristics of the hybrid passivation structure with various second passivation thicknesses: (a) gate-to-source capacitance; and (b) gate-to-drain capacitance.

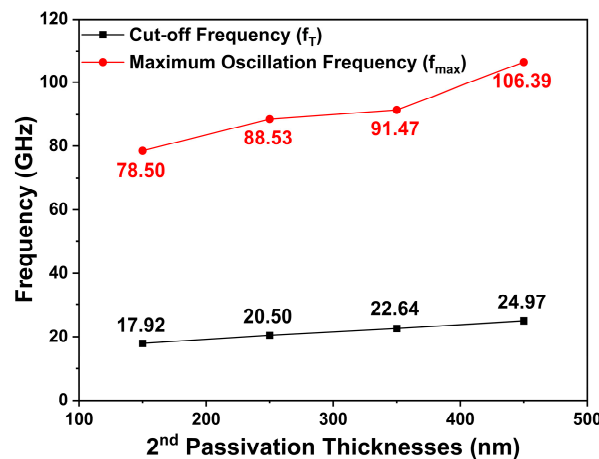


Figure 10. The simulated f_T and f_{max} as a function of the second passivation thicknesses at $V_{DS} = 20\text{ V}$ and $V_{GS} = -2.6\text{ V}$.

4. Discussion

In this article, we simulated the DC and RF characteristics of various passivation structures. Additionally, we analyzed the hybrid passivation structure by changing the second passivation thickness. Based on these results, we first calculated the LFOM and JFOM to investigate the performance of the device for the various passivation structures. Table 4 provides a summary of the DC and RF characteristics, including the figure-of-merit for the four different passivation structures. More precisely, the LFOM and JFOM of the basic Si_3N_4 passivation structures were 13.44 MW/mm and 5.73 THz-V, respectively. The HfO_2 passivation structure increased the LFOM by 48% and decreased the JFOM by 39% compared with the basic Si_3N_4 passivation structure. In comparison with the basic Si_3N_4

passivation structure, analysis of the hybrid passivation structure showed that the LFOM was increased by up to 35% and the JFOM was decreased by up to 4%.

Table 4. A summary of the DC and RF characteristics of various passivation structure HEMTs.

Parameters	Units	Si ₃ N ₄	HfO ₂	Hybrid	
First/second passivation thickness	nm	50/250	50/250	50/250	50/350
On-resistance (R_{on})	Ω -mm	4.02	3.84	3.97	4.16
Breakdown voltage (V_{BD})	V	232.47	276.27	268.41	267.57
Cut-off frequency (f_T)	GHz	24.64	10.17	20.50	22.64
Maximum oscillation frequency (f_{max})	GHz	110.27	48.72	88.53	91.47
Standard lateral figure-of-merit (LFOM)	MW/mm	13.44	19.93	18.15	17.21
Johnson's figure-of-merit (JFOM)	THz-V	5.73	2.81	5.50	6.06

Subsequently, the LFOM values for the hybrid passivation structure of different second passivation thicknesses were estimated to be 17.93, 18.15, 17.68, and 15.53 MW/mm, respectively. In addition, except for the hybrid passivation structure with 450-nm-thick second Si₃N₄ passivation, the LFOM values of the other hybrid passivation structures had improved by more than 28%, compared to the basic Si₃N₄ passivation structure. Further, we measured the JFOM values for the hybrid passivation structures of different second passivation thicknesses, which were 4.70, 5.50, 6.06, and 6.55 THz-V, respectively. As the second passivation thickness increased, the JFOM values also increased.

5. Conclusions

In this study, using TCAD simulation, we analyzed the operational characteristics of AlGaIn/GaN HEMTs in accordance with changes of passivation materials and thicknesses. Before analyzing the various passivation structures, all the simulation and material parameters were precisely set through mapping with the measurement data of the fabricated device to ensure the reliability of the simulated data. Based on the simulation results, we suggest an optimized hybrid structure of HEMT which adopts a 50-nm-thick first HfO₂ passivation and a 350-nm-thick second Si₃N₄ passivation. Unlike other general structures such as the field-plate in the HEMT, we confirmed that the hybrid passivation structure of the HEMT with suitable passivation thickness could enhance both the DC and RF performances, including the LFOM and JFOM. Consequently, the simulation results clearly show that HfO₂ as a passivation material with a second passivation thickness suitable for the AlGaIn/GaN HEMTs can be a promising candidate for future high-power and high-frequency applications.

Author Contributions: Conceptualization and writing—original draft preparation, J.-H.C.; software and investigation, W.-S.K.; formal analysis and data curation, D.K.; validation and formal analysis, J.-H.K.; formal analysis and investigation, J.-H.L.; validation and investigation, K.-Y.K.; validation and formal analysis, B.-G.M.; resources and investigation, D.M.K.; supervision, funding acquisition, resources, and writing—review and editing, H.-S.K. All authors have read and agreed to the published version of the manuscript.

Funding: This work was partly supported by an Institute of Information & Communications Technology Planning & Evaluation (IITP) grant funded by the government of the Republic of Korea (MSIT) under grant No. 2021-0-00760, as well as the Institute of Civil Military Technology Cooperation, funded by the Defense Acquisition Program Administration and the Ministry of Trade, Industry and Energy of the government of the Republic of Korea, under grant No. 22-CM-15.

Conflicts of Interest: The authors declare no conflict of interest.

References

1. Zhang, N.Q.; Keller, S.; Parish, G.; Heikman, S.; DenBaars, S.P.; Mishra, U.K. High breakdown GaN HEMT with overlapping gate structure. *IEEE Electron Device Lett.* **2000**, *21*, 421–423. [[CrossRef](#)]
2. Meneghini, M.; Rossetto, I.; Santi, C.D.; Rampazzo, F.; Tajalli, A.; Barbato, A.; Ruzzarin, M.; Borga, M.; Canato, E.; Zanoni, E.; et al. Reliability and failure analysis in power GaN-HEMTs: An overview. In Proceedings of the IEEE International Reliability Physics Symposium (IRPS), Monterey, CA, USA, 2–6 April 2017.
3. Mishra, U.K.; Shen, L.; Kazior, T.E.; Wu, Y.F. AlGaIn/GaN HEMTs—an overview of device operation and applications. *Proc. IEEE* **2002**, *90*, 1022–1031. [[CrossRef](#)]
4. Del Alamo, J.A.; Joh, J. GaN HEMT reliability. *Microelectron. Reliab.* **2009**, *49*, 1200–1206. [[CrossRef](#)]
5. Kim, J.G.; Cho, C.; Kim, E.; Hwang, J.S.; Park, K.H.; Lee, J.H. High Breakdown Voltage and Low-Current Dispersion in AlGaIn/GaN HEMTs with High-Quality AlN Buffer Layer. *IEEE Trans. Electron Devices* **2021**, *68*, 1513–1517. [[CrossRef](#)]
6. Sodan, V.; Oprins, H.; Stoffels, S.; Baelmans, M.; Wolf, I.D. Influence of Field-Plate Configuration on Power Dissipation and Temperature Profiles in AlGaIn/GaN on Silicon HEMTs. *IEEE Trans. Electron Devices* **2015**, *62*, 2416–2422. [[CrossRef](#)]
7. Saito, W.; Takada, Y.; Kuraguchi, M.; Tsuda, K.; Omura, I.; Omura, T. High breakdown voltage AlGaIn-GaN Power-HEMT design and high current density switching behavior. *IEEE Trans. Electron Devices* **2003**, *50*, 2528–2531. [[CrossRef](#)]
8. Shi, N.; Wang, K.; Zhou, B.; Weng, J.; Cheng, Z. Optimization AlGaIn/GaN HEMT with Field Plate Structures. *Micromachines* **2022**, *13*, 702. [[CrossRef](#)]
9. Saadat, O.I.; Chung, J.W.; Piner, E.L.; Palacios, T. Gate-First AlGaIn/GaN HEMT Technology for High-Frequency Applications. *IEEE Electron Device Lett.* **2009**, *30*, 1254–1256. [[CrossRef](#)]
10. Ahsan, S.A.; Ghosh, S.; Sharma, K.; Dasgupta, A.; Khandelwal, S.; Chauhan, Y.S. Capacitance modeling in dual field-plate power GaN HEMT for accurate switching behavior. *IEEE Trans. Electron Devices* **2015**, *63*, 565–572. [[CrossRef](#)]
11. Kwak, H.T.; Chang, S.B.; Kim, H.J.; Jang, K.W.; Yoon, H.S.; Lee, S.H.; Lim, J.W.; Kim, H.S. Operational Improvement of AlGaIn/GaN High Electron Mobility Transistor by an Inner Field-Plate Structure. *Appl. Sci.* **2018**, *8*, 974. [[CrossRef](#)]
12. Sohel, S.H.; Xie, A.; Beam, E.; Xue, H.; Razzak, T.; Bajaj, S.; Cao, Y.; Lee, C.; Lu, W.; Rajan, S. Polarization Engineering of AlGaIn/GaN HEMT With Graded InGaIn Sub-Channel for High-Linearity X-Band Applications. *IEEE Electron Device Lett.* **2019**, *40*, 522–525. [[CrossRef](#)]
13. Liu, X.; Chiu, H.C.; Liu, C.H.; Kao, H.L.; Chiu, C.W.; Wang, H.C.; Ben, J.; He, W.; Huang, C.R. Normally-off p-GaN Gated AlGaIn/GaN HEMTs Using Plasma Oxidation Technique in Access Region. *IEEE J. Electron Devices Soc.* **2020**, *8*, 229–234. [[CrossRef](#)]
14. Kuzmik, J.; Pozzovivo, G.; Abermann, S.; Carlin, J.; Gonschorek, M.; Feltn, E.; Grandjean, N.; Bertagnolli, E.; Strasser, G.; Pogany, D. Technology and Performance of InAlN/AlN/GaN HEMTs with Gate Insulation and Current Collapse Suppression Using ZrO₂ or HfO₂. *IEEE Trans. Electron Devices* **2008**, *55*, 937–941. [[CrossRef](#)]
15. Coltrin, M.E.; Baca, A.G.; Kaplar, R.J. Analysis of 2D transport and performance characteristics for lateral power devices based on AlGaIn alloys. *ECS J. Solid State Sci. Technol.* **2017**, *6*, S3114–S3118. [[CrossRef](#)]
16. Downey, B.P.; Meyer, D.J.; Katzer, D.S.; Roussos, J.A.; Pan, M.; Gao, X. SiN_x/InAlN/AlN/GaN MIS-HEMTs with 10.8THzV Johnson Figure of Merit. *IEEE Electron Device Lett.* **2014**, *35*, 527–529. [[CrossRef](#)]
17. Sanyal, I.; Lin, E.; Wan, Y.; Chen, K.; Tu, P.; Yeh, P.; Chyi, J. AlInGaIn/GaN HEMTs with High Johnson's Figure-of-Merit on Low Resistivity Silicon Substrate. *IEEE J. Electron Devices Soc.* **2020**, *9*, 130–136. [[CrossRef](#)]
18. Yoon, H.S.; Min, B.G.; Lee, J.M.; Kang, D.M.; Ahn, H.K.; Kim, H.; Lim, J. Microwave Low-Noise Performance of 0.17 μm Gate-Length AlGaIn/GaN HEMTs on SiC with Wide Head Double-Deck T-Shaped Gate. *IEEE Electron Device Lett.* **2016**, *37*, 1407–1410. [[CrossRef](#)]
19. Silvaco. Material Dependent Physical Models. In *Atlas User's Manual Device Simulation Software*; Silvaco Inc.: Santa Clara, CA, USA, 2016; pp. 519–523.
20. Kim, H.J.; Jang, K.W.; Kim, H.S. Operational Characteristics of Various AlGaIn/GaN High Electron Mobility Transistor Structures Concerning Self-Heating Effect. *J. Nanosci. Nanotechnol.* **2019**, *19*, 6016–6022. [[CrossRef](#)]
21. Raja, P.V.; Subramani, N.K.; Gaillard, F.; Bouslama, M.; Sommet, R.; Nallatamby, J. Identification of Buffer and Surface Traps in Fe-Doped AlGaIn/GaN HEMTs Using Y21 Frequency Dispersion Properties. *Electronics* **2021**, *10*, 3096. [[CrossRef](#)]
22. Vitanov, S.; Palankovski, V.; Maroldt, S.; Quay, R. High-temperature modeling of algan/gan hemts. *Solid-State Electron.* **2010**, *54*, 1105–1112. [[CrossRef](#)]
23. Lee, J.H.; Choi, J.H.; Kang, W.S.; Kim, D.; Min, B.G.; Kang, D.M.; Choi, J.H.; Kim, H.S. Analysis of Operational Characteristics of AlGaIn/GaN HEMT with Various Slant-Gate-Based Structures: A Simulation Study. *Micromachines* **2022**, *13*, 1957. [[CrossRef](#)] [[PubMed](#)]
24. Belkacemi, K.; Hocine, R. Efficient 3D-TLM modeling and simulation for the thermal management of microwave AlGaIn/GaN HEMT used in high power amplifiers SSPA. *J. Low Power Electron Appl.* **2018**, *8*, 23. [[CrossRef](#)]
25. Brady, R.G.; Oxley, C.H.; Brazil, T.J. An Improved Small-Signal Parameter-Extraction Algorithm for GaN HEMT Devices. *IEEE Trans. Microw. Theory Tech.* **2008**, *56*, 1535–1544. [[CrossRef](#)]
26. Yoon, H.S.; Min, B.G.; Lee, J.M.; Kang, D.M.; Ahn, H.K.; Kim, H.C.; Lim, J.W. Wide head T-shaped gate process for low-noise AlGaIn/GaN HEMTs. In Proceedings of the CS MANTECH Conference, Scottsdale, AZ, USA, 18–21 May 2015.

27. Saito, W.; Nitta, T.; Kakiuchi, Y.; Saito, Y.; Tusda, K.; Omura, I.; Yamaguchi, M. On-Resistance Modulation of High Voltage GaN HEMT on Sapphire Substrate Under High Applied Voltage. *IEEE Electron Device Lett.* **2007**, *28*, 676–678. [[CrossRef](#)]
28. Nuttinck, S.; Gebara, E.; Laskar, J.; Harris, H.M. Study of self-heating effects, temperature-dependent modeling, and pulsed load-pull measurements on GaN HEMTs. *IEEE Trans. Microw. Theory Tech.* **2001**, *49*, 2413–2420. [[CrossRef](#)]
29. Cioni, M.; Zagni, N.; Selmi, L.; Meneghesso, G.; Meneghini, M.; Zanoni, E.; Chini, A. Electric Field and Self-Heating Effects on the Emission Time of Iron Traps in GaN HEMTs. *IEEE Trans. Electron Devices* **2021**, *68*, 3325–3332. [[CrossRef](#)]
30. Jang, K.W.; Hwang, I.T.; Kim, H.J.; Lee, S.H.; Lim, J.W.; Kim, H.S. Thermal analysis and operational characteristics of an AlGaIn/GaN High electron mobility transistor with copper-filled structures: A simulation study. *Micromachines* **2019**, *11*, 53. [[CrossRef](#)]
31. Kabemura, T.; Ueda, S.; Kawada, Y.; Horio, K. Enhancement of Breakdown Voltage in AlGaIn/GaN HEMTs: Field Plate Plus High- k Passivation Layer and High Acceptor Density in Buffer Layer. *IEEE Trans. Electron Devices* **2018**, *65*, 3848–3854. [[CrossRef](#)]
32. Hanawa, H.; Onodera, H.; Nakajima, A.; Horio, K. Numerical Analysis of Breakdown Voltage Enhancement in AlGaIn/GaN HEMTs with a High- k Passivation Layer. *IEEE Trans. Electron Devices* **2014**, *61*, 769–775. [[CrossRef](#)]
33. Cheng, J.; Rahman, M.W.; Xie, A.; Xue, H.; Soheli, S.H.; Beam, E.; Lee, C.; Yang, H.; Wang, C.; Cao, Y.; et al. Breakdown Voltage Enhancement in ScAlN/GaN High-Electron-Mobility Transistors by High- k Bismuth Zinc Niobate Oxide. *IEEE Trans. Electron Devices* **2021**, *68*, 3333–3338. [[CrossRef](#)]
34. Chung, J.W.; Hoke, W.E.; Chumbes, E.M.; Palacios, T. AlGaIn/GaN HEMT with 300-GHz f_{max} . *IEEE Electron Device Lett.* **2010**, *31*, 195–197. [[CrossRef](#)]

Disclaimer/Publisher’s Note: The statements, opinions and data contained in all publications are solely those of the individual author(s) and contributor(s) and not of MDPI and/or the editor(s). MDPI and/or the editor(s) disclaim responsibility for any injury to people or property resulting from any ideas, methods, instructions or products referred to in the content.